



OPEN

Preparation and adsorption properties of magnetic chitosan/sludge biochar composites for removal of Cu^{2+} ions

Meng Zhang, Yunqing Liu[✉], Zhizhen Yin[✉], Dan Feng & Hui Lv

The magnetic chitosan/sludge biochar composite adsorbent was prepared using chitosan, Fe_3O_4 , and sludge biochar as raw materials. The composite adsorbent was able to achieve rapid solid–liquid separation under an applied magnetic field. The morphology and microstructure of the composite adsorbent were characterized by FTIR, XRD, SEM, VSM, and BET analysis. The adsorption performance of the composite adsorbent on Cu^{2+} was investigated through static adsorption experiments, and the effects of adsorbent dosage, initial concentration of Cu^{2+} , initial pH of the solution, and adsorption temperature on the adsorption efficiency of Cu^{2+} were discussed. The results showed that chitosan and Fe_3O_4 were successfully loaded on sludge biochar. When the initial concentration of Cu^{2+} was 30 mg/L, the dosage of the magnetic chitosan/sludge biochar composite material was 0.05 g, the adsorption time was 180 min, pH was 5, and the temperature was room temperature, the maximum removal rate of Cu^{2+} reached 99.77%, and the maximum adsorption capacity was 55.16 mg/g. The adsorption kinetics and adsorption isotherm data fitted well with the pseudo-second-order kinetic model and Langmuir adsorption isotherm model, indicating that the adsorption process was chemisorption with monolayer coverage.

With the rapid growth of the Chinese economy and the flourishing development of various industries, numerous types of pollution have emerged. Among these, the issue of heavy metal pollution in water bodies has always been a focal point of concern as well as a challenging problem in water pollution control. Wastewater containing heavy metals generated during industrial production processes, such as mining, mechanical manufacturing, and the chemical industry, is one of the most significant sources of pollution in water bodies. These pollutants pose a severe threat to human life and health. Heavy metals, including Cr^{6+} , Pb^{2+} , Hg^{2+} , V^{2+} , and Cu^{2+} , are particularly harmful contaminants found in water bodies. Among them, water pollution caused by Cu^{2+} primarily originates from industries such as electroplating, non-ferrous metal processing, and copper mining. When the copper concentration in water reaches 0.01 mg/L, it significantly hinders the self-purification process of water bodies. At levels exceeding 3.0 mg/L, it generates an unpleasant odor, and when the concentration exceeds 15 mg/L, the water becomes unfit for consumption¹. The United States Environmental Protection Agency (EPA) has set the allowable limit of Cu^{2+} in industrial wastewater at 1.3 mg per liter. Additionally, the World Health Organization (WHO) has established the allowable limit of Cu^{2+} in drinking water at 1.5 mg/L². Consequently, it is crucial to develop more efficient and environmentally friendly adsorbent materials to tackle Cu^{2+} pollution in water bodies.

There are many methods for removing heavy metals from polluted water bodies, including chemical precipitation, electrochemical methods, membrane separation, ion exchange, biological methods, and adsorption, etc³. Among them, adsorption has the advantages of simple operation, good effect, clean process, easy regeneration, and no secondary pollution, making it one of the most promising technologies for heavy metal wastewater treatment. However, commonly used adsorbents such as activated carbon, zeolite, and natural clay have low adsorption capacity and poor adsorption selectivity, which often result in unsatisfactory results in the treatment of heavy metal wastewater.

Currently, the total amount of sludge produced by urban sewage treatment plants in China has been rapidly increasing at a growth rate exceeding 10% since 2007. The sludge contains a high content of organic matter (30% ~ 70%) and is inexpensive and readily available. Utilizing sludge to produce biochar is considered a promising disposal method⁴. Sludge biochar is a solid material generated from the anaerobic or oxygen-limited

Key Laboratory of Pollutant Chemistry and Environmental Treatment, School of Resources and Environment, Yili Normal University, Xinjiang 835000, Yining, China. ✉email: liuyq151@nenu.edu.cn; yinzhizhen123@163.com

high-temperature pyrolysis of sludge. Due to its abundant pore structure, aromatic layer structure, and low cost, biochar is regarded as a novel adsorbent with great potential in the field of water treatment.

Chitosan is a natural alkaline polysaccharide and is the product of deacetylation of chitin⁵. Chitosan molecules contain many hydroxyl and amino groups, which can form hydrogen bonds, electrostatic interactions, and van der Waals forces with heavy metal ions, thereby achieving the purpose of adsorbing heavy metal ions. Chitosan is widely used in the removal of heavy metal ions due to its advantages such as biodegradability, antibacterial properties, hydrophilicity, renewability, and environmental friendliness. To enhance adsorption performance, magnetic adsorbents such as Fe₃O₄ magnetic particles and nanoparticles are often loaded on the surface of chitosan and applied in the treatment of heavy metal wastewater⁶.

Chao et al.⁷ prepared chitosan-modified magnetic nanoparticles using a reverse suspension cross-linking method to address the issue of molybdenum exceeding the standard in mining wastewater. This material was used to adsorb molybdenum (VI) from water, and the results showed that the theoretical maximum adsorption capacity was determined to be 35.54 mg/g. Even after three cycles of regeneration, the adsorption rate of chitosan-modified magnetic nanoparticles for Mo (VI) remained above 90%. The chitosan-modified magnetic nanoparticles are a fast and efficient method for removing Mo (VI). They have good reusability, strong magnetic properties, and are suitable for solid–liquid magnetic separation.

Zheng et al.⁸ synthesized recyclable magnetic biochar functionalized with chitosan and ethylenediamine-tetraacetic acid (E-CMBC) to investigate its adsorption performance for Pb (II) in aqueous solutions and the underlying potential adsorption mechanism. The results showed that under pH 3.0 conditions, the removal rate of Pb (II) was significantly increased to 156.68 mg/g compared to the unmodified original biochar (10.90 mg/g). The magnetic intensity of E-CMBC was measured to be 3.1 emu/g, suggesting that the consumed E-CMBC could be separated from water using an external magnet. Regeneration studies showed that after three cycles of adsorption–desorption, the recovery rate of the adsorbent was 78.60%, and the adsorption capacity retention rate was 97.26%. In conclusion, E-CMBC is a novel, recyclable, and efficient adsorbent for Pb (II) removal.

Li et al.⁹ prepared amino-thiourea modified chitosan-magnetic biochar composite (TMBC) for the efficient removal of Cd (II) from wastewater. The synthesized material was characterized and its adsorption mechanism and thermodynamics were extensively studied. Adsorption experiments revealed that TMBC exhibited higher affinity for Cd (II) compared to magnetic biochar composite, biochar, and other carbon-based adsorbents. The adsorption process of Cd (II) followed a pseudo-second-order kinetic model. The maximum adsorption capacities based on the Langmuir model at 298, 308, and 318 K were 93.72, 121.9, and 137.3 mg/g, respectively. Kang et al.¹⁰ prepared sewage sludge-based biochar loaded with nanoscale zero-valent iron (NZVI) under 700 °C (nBC700) conditions for the removal of Cr (VI) and Cu (II). The results showed that the addition of NZVI greatly enhanced the adsorption capacity of biochar for Cu (II) and Cr (VI), with increases of 251.96% and 205.18%, respectively.

In summary, it is particularly important to find an adsorbent with high adsorption capacity, economical, and environmentally friendly for treating wastewater contaminated with heavy metals. Using dehydrated sludge as raw material, converting it into sludge-based biochar through high-temperature pyrolysis, preparing highly efficient composite materials by loading a small amount of CTS and Fe₃O₄, and selectively using them for treating heavy metal wastewater not only improves the added value of the sludge-based biochar, but also makes the prepared composite adsorbent have a certain degree of magnetism. The sludge was separated from water by applying an external magnetic field to reduce the secondary pollution of water bodies. Meanwhile, the chitosan on the surface of the composite material has active groups such as amino and hydroxyl groups, and the nano-magnetic powder contained in the composite material has a large specific surface area and is uniformly attached to the surface of the sludge biochar, which improves the adsorption performance. By studying the optimal conditions for the adsorption of heavy metal ions by composite materials, it provides an important theoretical foundation and scientific basis for more efficient removal of heavy metal ions from wastewater.

In this paper, a composite material was prepared using chitosan (CTS), iron (III) oxide (Fe₃O₄), and sewage sludge-based biochar (SBC). FTIR, XRD, SEM, VSM, and BET techniques were employed to characterize their functional groups, structures, morphologies, magnetic properties, specific surface areas, and pore volumes. The effect of magnetic chitosan/sludge-based biochar (Fe₃O₄@CTS/SBC) composites on the removal of Cu²⁺ from simulated wastewater was investigated by controlling variables such as initial concentration of Cu²⁺, adsorbent dosage, pH, temperature and other adsorption properties. The adsorption characteristics of Fe₃O₄@CTS/SBC on Cu²⁺ were investigated by adsorption isotherms, adsorption kinetics and adsorption thermodynamics.

Material and methods

Reagents and materials

All chemical reagents were of analytical grade, and the solutions used in this study were prepared with deionized water. Chitosan was purchased from Shanghai Aladdin Biochemical Technology Co., Ltd; Iron oxide was purchased from Beijing Nan Shang Le Chemical Factory; Glutaraldehyde 50%, sodium hydroxide and hydrochloric acid were purchased from Tianjin Fuchen Chemical Reagent Factory; Acetic acid and ammonia solution were purchased from Tianjin Beilian Fine Chemical Development Co., Ltd; 1,3-dicyclohexyl-2-methylidene-carboxamide was purchased from Xi'an Chemical Reagent Factory; Anhydrous ethanol and anhydrous copper sulfate were purchased from Tianjin Damao Chemical Reagent Factory; Triethylenetetramine citrate was purchased from Shanghai Sihewi Chemical Co., Ltd.

Preparation method of adsorbent

Preparation of Sewage Sludge Biochar (SBC)

Sludge biochar (SBC) was prepared from the remaining sludge of a sewage treatment plant in Yining City. The sludge was first placed under ventilated conditions to dry naturally drying. It was then thoroughly ground and screened through an 80-mesh sieve size for later use. Next, an appropriate amount of dried sludge was removed from the pretreated sludge and placed in a crucible. The crucible was sealed with tin foil and placed in a muffle furnace for pyrolysis by thermal cracking. The pyrolysis process consisted of seven steps: 20 °C to 200 °C, heating time 1 h, holding time 1 h at 200 °C; 200 °C to 300 °C, heating time 1 h, holding time 1 h at 300 °C; 300 °C to 400 °C heating time 1 h, holding time 1 h at 400 °C; 400 °C to 500 °C, heating time 1 h, holding time 1 h at 500 °C; 500 °C to 300 °C, cooling time half an hour; 300 °C to 200 °C, cooling time half an hour; and 200 °C to 25 °C, cooling time half an hour. This process produced the desired sewage sludge biochar. In order to remove the excess inorganic substances and ash content, the sewage sludge biochar was treated by acid washing with dilute hydrochloric acid (biochar: dilute hydrochloric acid) in the ratio of 1:10. After stirring on a magnetic stirrer for 1 h, the mixture was filtered and washed with water until neutral. Finally, the biochar was dried and reserved for further use.

Preparation of magnetic chitosan (Fe_3O_4 @CTS/SBC)

0.5 g of chitosan powder was weighed using an analytical balance and added to 20 mL of acetic acid at 2% volume fraction. The mixture was stirred thoroughly at room temperature with a magnetic stirrer until chitosan was completely dissolved to obtain chitosan acetic acid solution. Added 0.2 g Fe_3O_4 and stirred well, ultrasonicated for 30 min and dispersed evenly. Added 3 mL of 25% glutaraldehyde and placed the reaction mixture in a 50 °C water bath for cross-linking reaction for 1 h. After completion of the cross-linking reaction, the pH was adjusted to 8 by gradually dropping NaOH solution. Further cross-linking reaction was carried out by continuing heating in a water bath at 65 °C for one hour. Finally, it was washed with distilled water until the pH reached 7. The precipitate was collected and transferred to a vacuum drying oven at 65 °C until reached a constant weight. This will yield magnetic chitosan.

Preparation of magnetic chitosan/sludge biochar composite material

0.5 g of chitosan was weighed and dissolved in 250 mL of aqueous acetic acid solution with a volume fraction of 1%. The solution was stirred at room temperature until completely dissolved. The pH was adjusted to 6 with a NaOH solution of 20% by mass. Slowly poured the chitosan solution into 0.5 g of sludge biochar and placed it in a water bath at 60 °C with stirring for 4 h. After 4 h, slowly added 0.5 g of Fe_3O_4 magnetic fluid (prepared by dispersing 0.5 g of Fe_3O_4 particles in 100 mL of distilled water) to the mixture. The reaction was continued for 1 h. The resulting product was washed with distilled water until the supernatant was neutral. The product was placed in a vacuum drying oven at 65 °C and dried thoroughly. The dried product was thoroughly ground and stored for future use.

Experimental methods

Determination of Cu^{2+} ions

This method is an improved double-ring ketone oxime (BCO) spectrophotometric method based on the dual aldehyde carbonyl oxime spectrophotometric method of China's "Standard Test Method for Drinking Water" (GB/T5750-2006)^{11,12}. In this method, aliquots of 0.0 mL, 0.1 mL, 0.2 mL, 0.4 mL, 0.8 mL, 1.2 mL, and 2.0 mL of the copper standard solution were transferred into seven 10 mL colorimetric tubes using a pipette. The color reagent was added sequentially according to the dual acetylacetone oxime (BCO) spectrophotometric method and then distilled water was added at the calibration line. The mixture was thoroughly mixed and allowed to stand for 15 min. The absorbance was measured using a visible spectrophotometer at a wavelength of 600 nm and a 5 cm cuvette with distilled water as reference. The Cu^{2+} standard curve was obtained by taking the measured absorbance as the vertical coordinate and the concentration of Cu^{2+} standard solution as the horizontal coordinate, from which the concentration of Cu^{2+} in the solution could be calculated.

Characterization of SBC and Fe_3O_4 @CTS/SBC

Powdered sludge biochar (SBC) and magnetic chitosan-modified sludge biochar (Fe_3O_4 @CTS/SBC) composites were characterized by X-ray diffractometer. The scanning angles for both samples were in the range of 10°–80° with a step size of 0.02° and a scanning speed of 10°/min. Fourier transform infrared (FTIR) spectroscopy was carried out on the samples of SBC, Fe_3O_4 @CTS, Fe_3O_4 @CTS/SBC in the range of wave numbers from 500 cm^{-1} to 4000 cm^{-1} . The morphology and structure of the samples were observed using a scanning electron microscope after dispersing the samples in ethanol solution at an accelerating voltage of 3 kV. The magnetic properties of the composite adsorbent were investigated by measuring the hysteresis return line of Fe_3O_4 @CTS/SBC using a vibrating sample magnetometer (VSM). The specific surface area and pore size analysis of the samples were performed under normal temperature and pressure conditions. The samples weighed 0.3 g and were subjected to N_2 gas adsorption–desorption at a desorption temperature of 200 °C for approximately 6 h. The p/p_0 values were in the range of 0.05 and 0.99, and BET calculations were used to determine the specific surface area. The pore size distribution of mesoporous materials was analyzed using the BJH model.

Single factor influence experiment

In this study, the effects of composite adsorbent dosage, initial concentration of Cu^{2+} , pH and adsorption temperature on the adsorption effect were investigated. The fixed wastewater volume was 30 mL, the temperature of the shaking table was 25 °C, the rotational speed was 180r/min, and the adsorption time was 180 min, and

the adsorption time was static. The supernatant was filtered with a 0.45 μm filter tip, and 2 mL of the filtrate was placed in a 10 mL colorimetric tube, and equal amounts of tri-ammonium citrate, pH 9 buffer, and BCO solution were added with the production standard. The absorbance was measured at 600 nm by visible spectrophotometer to determine the optimum conditions for adsorption of Cu²⁺.

Analysis and calculation

The adsorption performance of the composites was evaluated using modified chitosan/sludge biochar as adsorbent. The effects of initial concentration of Cr (VI) ions, pH, temperature and adsorbent dosage on the adsorption performance of heavy metal ions were determined by batch tests. The adsorption rate (R) and adsorption capacity (q) were calculated using Eqs. (1) and (2).

$$R = \frac{C_0 - C_e}{C_0} \quad (1)$$

$$Q = \frac{(C_0 - C_e)V}{m} \quad (2)$$

where R is the adsorption rate, expressed as a percentage (%); Q is the adsorption capacity in mg/g; C₀ represents the initial mass concentration of Cu²⁺ ions in the simulated wastewater in mg/L; C_e is the mass concentration of the equilibrium state of the Cu²⁺ ions after adsorption in mg/L; V represents the volume of simulated wastewater in mL; and m represents the mass of the adsorbent in grams (g).

Adsorption kinetics research

Adsorption kinetics models are used to investigate the mechanism of adsorption processes at the solid–liquid interface¹³. Commonly used kinetic models include pseudo-first-order adsorption rate equation¹⁴, pseudo-second-order adsorption rate equation¹⁵, and Weber-Morris intra-particle diffusion model¹⁶, which are used to explore the interaction mechanism between the adsorbent and the adsorbate.

Pseudo-first-order kinetic model equation:

$$\ln(q_e - q_t) = \ln q_{e,1} - k_1 t \quad (3)$$

where q_e and q_t represent the adsorption amounts at equilibrium and at time t, respectively, in mg/g; q_{e,1} is the theoretical equilibrium adsorbed amount calculated from the pseudo-first-order kinetic rate equation in mg/g; k₁ is the rate constant of the pseudo-first-order adsorption in min⁻¹; plotting ln (q_e - q_t) against t, the slope and intercept can be used to calculate k₁ and q_{e,1}.

Pseudo-second-order kinetic model equation:

$$\frac{t}{q_t} = \frac{1}{k_2 q_{e,2}^2} + t/q_e \quad (4)$$

where q_t represents the adsorption amount at time t in mg/g; q_{e,2} represents the theoretical equilibrium adsorption amount calculated from the pseudo-second-order kinetic rate equation in mg/g; k₂ is the rate constant of the pseudo-second-order adsorption in g/(mg·min). Plotting t on the x-axis and t/q_t on the y-axis, the slope and intercept can be used to calculate q_{e,2} and k₂.

Weber-Morris intra-particle diffusion model:

$$q_t = k_p t^{1/2} + C \quad (5)$$

where q_t represents the adsorption amount at time t in mg/g; k_p represents the intra-particle diffusion constant in mg/(g·min^{1/2}); C represents a constant related to the boundary layer thickness. Plotting t^{1/2} on the x-axis and q_t on the y-axis, the slope and intercept can be used to calculate k_p and C. If the fitted line passes through the origin, it indicates that the adsorption rate is solely affected by intra-particle diffusion. If the line does not pass through the origin, it suggests that intra-particle diffusion is not the only rate-controlling step in the adsorption process.

Boyd first-order dynamics model. For intraparticle diffusion, Boyd¹⁷ derived the intraparticle diffusion model (Boyd pseudo first model). Boyd's intraparticle diffusion model is based on Fick's second law of diffusion, which describes the change in particle concentration during diffusion. The model involves factors such as diffusion coefficients, diffusion rates and boundary conditions. According to different assumptions and boundary conditions, different forms of intraparticle diffusion models can be obtained. Boyd's intraparticle diffusion model provides a quantitative analytical tool for studying the diffusion behavior of particles. It can help us understand and predict the concentration distribution, rate, and interaction with the environment and boundary conditions of particles during internal diffusion. The intraparticle diffusion model can be derived by solving the diffusion partial differential equation and making assumptions according to different situations, and its linearization formula is as follows:

$$\ln\left(1 - \left(\frac{q}{q_e}\right)^2\right) = -k_i t \quad (6)$$

where k_i represents the apparent adsorption rate parameter.

Adsorption isotherm model

The adsorption equilibrium relationship between the adsorbent and the adsorbate was described using the Langmuir isotherm model and the Freundlich model¹⁸. The Langmuir isotherm model is suitable for the monolayer adsorption with uniformly distributed energy adsorption sites, and the adsorption model is as follows¹⁹:

$$\frac{C_e}{q_e} = \frac{1}{q_m K_L} + C_e/q_m \quad (7)$$

where q_e represents the equilibrium adsorption capacity in mg/g; q_m represents the maximum adsorption capacity in mg/g; c_e represents the equilibrium concentration in mg/L; k_L represents the adsorption rate constant in L/mg.

The Freundlich isotherm model is suitable for the multilayer adsorption on adsorbents with heterogeneous physicochemical properties. The expression for the Freundlich isotherm model is as follows²⁰:

$$\ln q_e = \frac{1}{n} \ln C_e + \ln K_F \quad (8)$$

where q_e represents the equilibrium adsorption capacity in mg/g; n is a constant related to the adsorption intensity; c_e represents the equilibrium concentration in mg/L; k_F represents the Freundlich adsorption rate constant in mg/g·(L/mg)^(-1/n).

The Temkin isotherm is used to describe the chemisorption process based on electrostatic force of positive and negative charges, and its expression is as follows:

$$q_e = \frac{RT}{b} \ln k_t + \frac{RT}{b} \ln c_e \quad (9)$$

where q_e represents the equilibrium adsorption capacity in mg/g; c_e represents the equilibrium concentration in mg/L; k_t is Temkin's constant; b is the heat-related adsorption constant.

Adsorption thermodynamics study

Adsorption thermodynamics focuses on the conversion relationship between macroscopic thermal phenomena and other forms of energy²¹. The spontaneity of the adsorption process can be determined by the Gibbs free energy change (ΔG). When $\Delta G < 0$, the adsorption process occurs spontaneously. When $\Delta G > 0$, it is a non-spontaneous. Whether the adsorption process is exothermic or endothermic can be determined by the enthalpy change (ΔH). When $\Delta H < 0$, the adsorption is exothermic in nature. On the contrary, it is heat-absorbing in nature. The Gibbs free energy change (ΔG), enthalpy change (ΔH) and entropy change (ΔS) are calculated by Eqs. (10) and (11).

$$\ln k = -\frac{\Delta H}{RT} + \frac{\Delta S}{R} \quad (10)$$

$$\Delta G = \Delta H - T\Delta S \quad (11)$$

where R represents the gas constant, 8.314 J/mol/k; T is the Kelvin temperature, K.

Results

Characterization of Adsorbent Materials

XRD analysis

XRD, also known as X-ray diffraction, is a technique used to analyze the crystal structure of different chemical substances. A unique x-ray diffraction pattern is produced by x-ray diffraction of the sample. In this study, SBC, Fe₃O₄@CTS and Fe₃O₄@CTS/SBC were analyzed by x-ray diffraction. The results are shown in Fig. 1.

Based on the XRD analysis, it could be determined that SBC mainly consists of calcite (CaCO₃), quartz (SiO₂), and cordierite (Mg, Fe₂(Al₄Si₅O₁₈)). The corresponding crystallographic indices (diffraction indices) for calcite are (012), (104), (110), (113), (202), (018), (116), (122), and (300); for quartz they are (100), (011), (110), (111), (200), (112), (121), and (203); and for cordierite they are (110), (002), (003), (020), (004), and (223). Therefore, these diffraction peaks could be observed in the XRD spectra of SBC and Fe₃O₄@CTS/SBC.

FT-IR analysis

FT-IR spectroscopy is used to study the structure of a sample and to determine the type of functional groups present. When a sample is exposed to infrared radiation of different wavelengths, it absorbs specific wavelengths, resulting in an infrared absorption spectrum of the substance²². The FT-IR spectra of SBC, Fe₃O₄@CTS, and Fe₃O₄@CTS/SBC composite adsorbents are shown in Fig. 2.

Sample SBC showed peaks at 874 cm⁻¹ and 1456 cm⁻¹, corresponding to the aromatic C-H and -COOH groups, respectively, which demonstrated that sludge biochar contains abundant oxygenated functional groups²³. Moreover, sample Fe₃O₄@CTS/SBC also showed a peak at 887 cm⁻¹, which indicated that the sludge biochar was formed by successful complexation with magnetic chitosan. Samples Fe₃O₄@CTS and Fe₃O₄@CTS/SBC showed peaks at 1382 cm⁻¹, which could be attributed to the C-H deformation vibrations of chitosan's -CH₃ group. The bending vibration absorption peak of -NH₂ usually occurs in the range of 1650–1560 cm⁻¹, and this functional group appeared at 1582 cm⁻¹ in the infrared spectra of Fe₃O₄@CTS and Fe₃O₄@CTS/SBC, which indicated the presence of -NH₂ bending vibration absorption peak in magnetic chitosan²⁴, which confirmed the existence of chitosan in the composites. Sample Fe₃O₄@CTS exhibited a characteristic absorption peak of Schiff base (-C=N-)

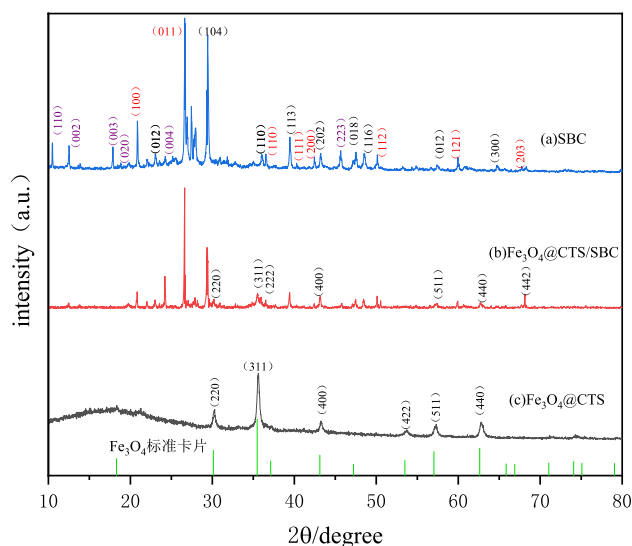


Figure 1. X-ray diffraction pattern of adsorbent.

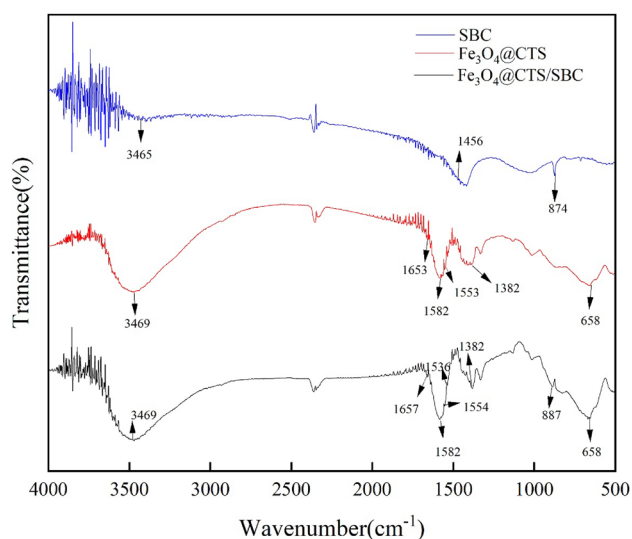


Figure 2. Infrared spectrogram of adsorbent.

at 1653 cm^{-1} , which indicated the participation of glutaraldehyde in cross-linking reaction. Both sample $\text{Fe}_3\text{O}_4@$ CTS (1653 cm^{-1}) and sample $\text{Fe}_3\text{O}_4@$ CTS/SBC (1657 cm^{-1}) showed characteristic absorption peaks corresponding to the stretching vibrations of the amide C=O group in $\text{Fe}_3\text{O}_4@$ CTS, which indicated the presence of chitosan in the composites²⁵. Peaks associated with the stretching vibration absorption of Fe–O appeared at 658 cm^{-1} in the spectra of $\text{Fe}_3\text{O}_4@$ CTS and $\text{Fe}_3\text{O}_4@$ CTS/SBC²⁶, which indicated the successful formation of Fe_3O_4 on chitosan and the magnetic properties of $\text{Fe}_3\text{O}_4@$ CTS/SBC.

SEM analysis

The Scanning Electron Microscope (SEM) is commonly used for observing the surface morphology of materials. In order to gain a more intuitive and clear understanding of the microstructure of SBC and $\text{Fe}_3\text{O}_4@$ CTS/SBC composite adsorbents, SEM analysis was performed on each sample. Figure 3a,b respectively showed the SEM images of SBC magnified 10,000 times and 20,000 times, while Fig. 4a,b respectively showed the SEM images of $\text{Fe}_3\text{O}_4@$ CTS/SBC composite adsorbent magnified 10,000 times and 20,000 times.

Specific surface area and pore size analysis

There are six common types of adsorption isotherms, as shown in Fig. 5. Type I is the most representative Langmuir isotherm, which is often observed in microporous materials. Type II is an S-shaped isotherm, mainly occurring on non-porous or macroporous solid surfaces. Type III is convex downward throughout the entire

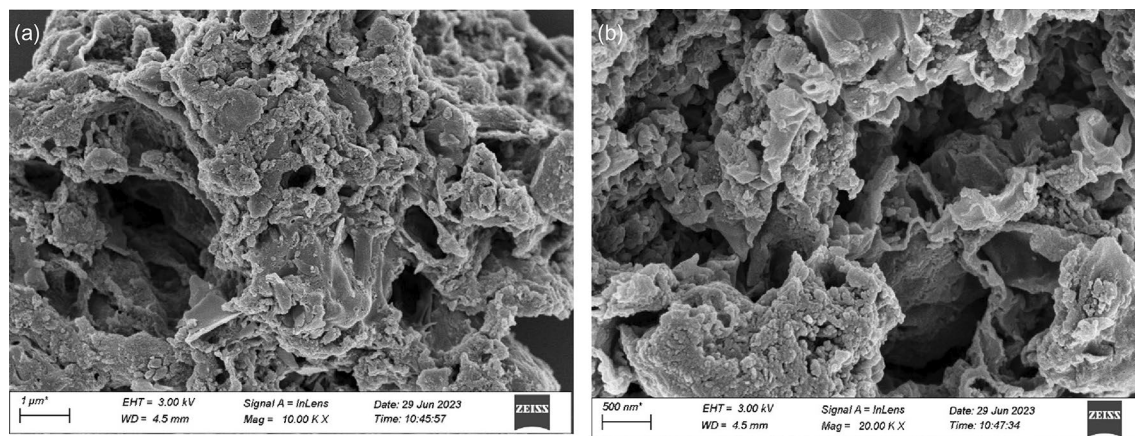


Figure 3. (a) SEM with 10,000 times SBC amplification, (b) SEM with 20,000 times SBC amplification.

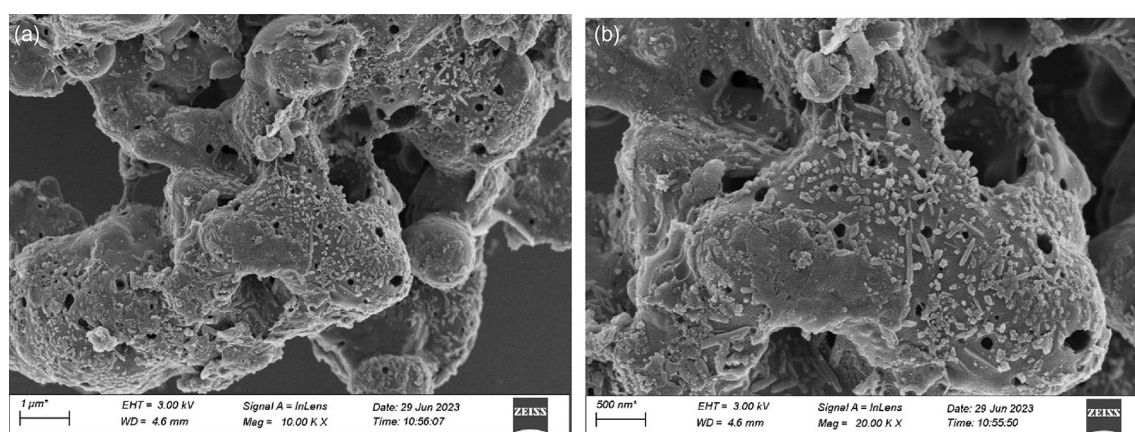


Figure 4. (a) $\text{Fe}_3\text{O}_4@$ CTS/SBC SEM with 10,000 times magnification, (b) $\text{Fe}_3\text{O}_4@$ CTS/SBC SEM with 20,000 times magnification.

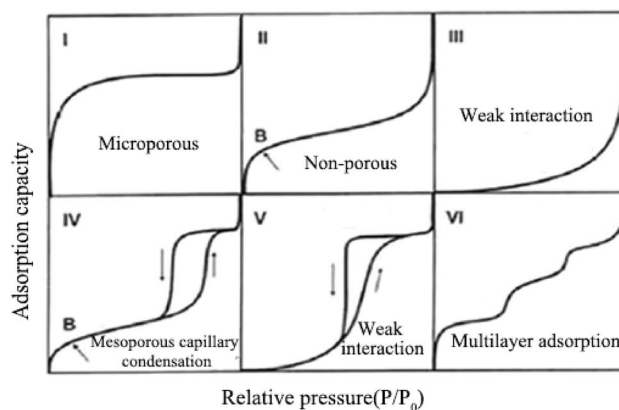


Figure 5. Adsorption isotherm type.

pressure range, with no inflection point. Type IV is similar to Type II, but in the low P/P_0 region, the curve is convex upward. Unlike Type III, Type V is characterized by a convex shape towards the relative pressure axis, and the presence of an inflection point at higher relative pressures. Type VI is well known for its stepped adsorption process, where the stepped shape is attributed to the sequential multilayer adsorption on non-porous surfaces.

The N_2 adsorption–desorption isotherms provide further insight into the properties of the adsorbent materials. In this study, the N_2 adsorption–desorption isotherms of SBC and $\text{Fe}_3\text{O}_4@$ CTS/SBC composite adsorbents were shown in Fig. 6. Table 1 showed the specific surface area and pore volume of $\text{Fe}_3\text{O}_4@$ CTS/SBC and SBC.

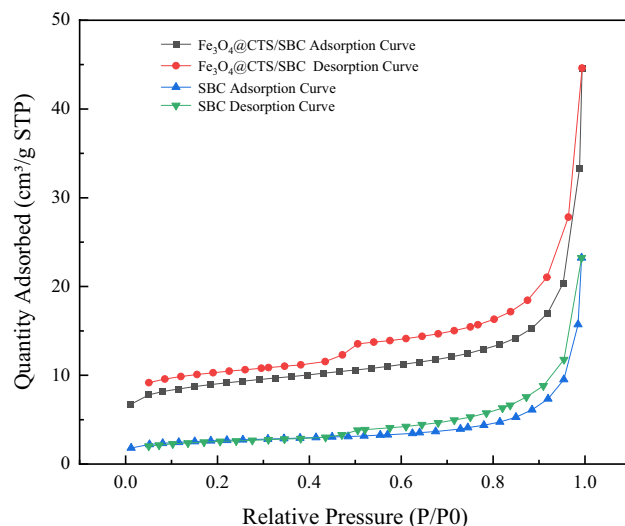


Figure 6. Adsorption and desorption isotherms of SBC and $\text{Fe}_3\text{O}_4@CTS/SBC$.

Sample	Specific surface area/(m^2/g)	Pore volume /(cm^3/g)
	ABET	V_{total}
SBC	9.33	0.0143
$\text{Fe}_3\text{O}_4@CTS/SBC$	32.86	0.0311

Table 1. Surface structure parameters of adsorbent.

The pore size distribution of SBC and $\text{Fe}_3\text{O}_4@CTS/SBC$ composite adsorbents could be observed from Fig. 7, which mainly lied between 2 to 50 nm, indicating that they are mesoporous materials. The figure also showed that the pore volume of the composite adsorbent is larger than that of sludge biochar.

Magnetic performance analysis

The magnetization intensity is an important factor for the solid–liquid separation after the adsorbent has completed the adsorption process. To study the magnetic properties of $\text{Fe}_3\text{O}_4@CTS/SBC$ composites, the magnetic hysteresis line of $\text{Fe}_3\text{O}_4@CTS/SBC$ was measured at room temperature, and the result were shown in Fig. 8a: The magnetic hysteresis line of $\text{Fe}_3\text{O}_4@CTS/SBC$ composites showed an "S"-shaped curve. During the magnetization process, the magnetization intensity of the composites increased with the increased of the applied magnetic field

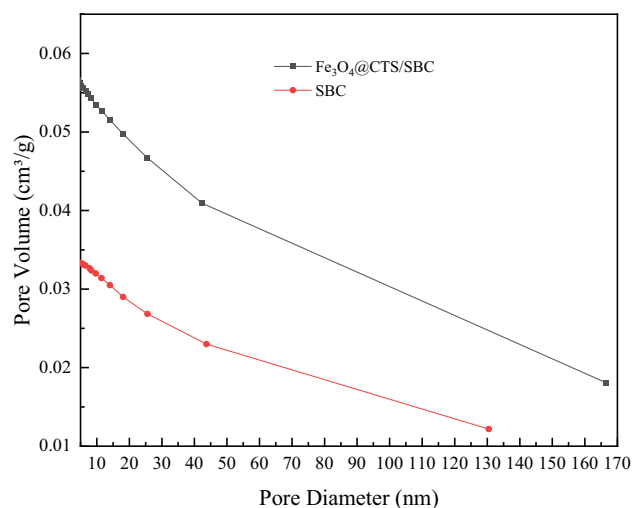


Figure 7. Aperture distribution of SBC and $\text{Fe}_3\text{O}_4@CTS/SBC$.

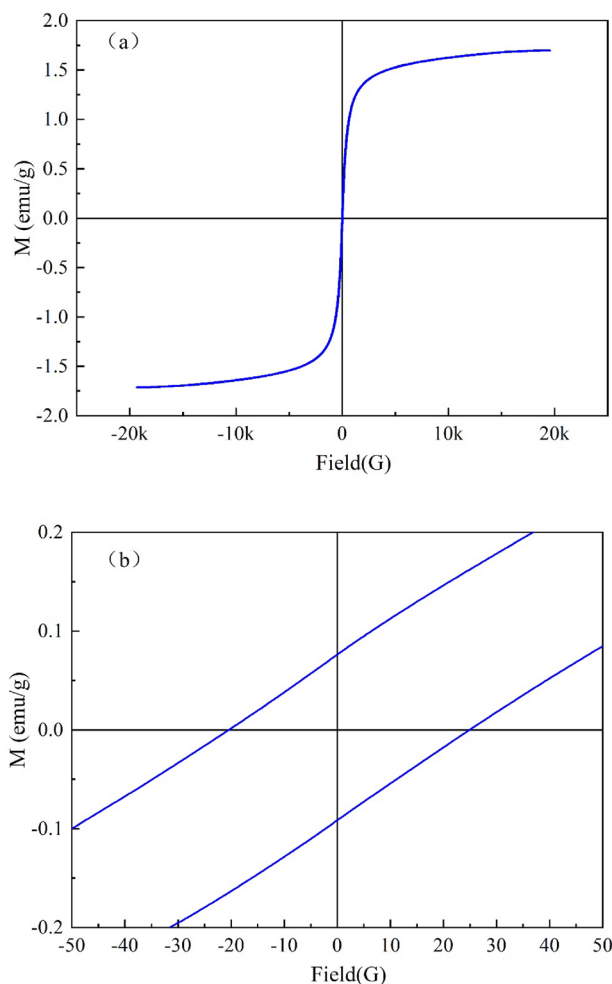


Figure 8. (a) Hysteresis loop of $\text{Fe}_3\text{O}_4@CTS/SBC$ composite (b) coercivity curve of $\text{Fe}_3\text{O}_4@CTS/SBC$ composite.

strength and ultimately reached saturation. $\text{Fe}_3\text{O}_4@CTS/SBC$ composites exhibited magnetism with a saturation magnetization intensity of 1.71 emu/g. Figure 8b showed that the composites had large coercivity of 25 Oe, which indicated strong ferromagnetism. The composites could be separated from the aqueous solution by applying an external magnetic field.

Single factor impact experiment

(1) The effect of $\text{Fe}_3\text{O}_4@CTS/SBC$ composites dosage on Cu^{2+} adsorption efficiency: The experimental results were shown in Fig. 9.

According to Fig. 9, the adsorption efficiency of $\text{Fe}_3\text{O}_4@CTS/SBC$ composites increased with the increased in the dosage of $\text{Fe}_3\text{O}_4@CTS/SBC$ composites. However, when the dosage exceeded 0.03 g, the increased in adsorption efficiency became slower.

(2) The effect of initial Cu^{2+} concentration on the adsorption performance: The experimental results were shown in Fig. 10.

From Fig. 10, the adsorption capacity of $\text{Fe}_3\text{O}_4@CTS/SBC$ composites for Cu^{2+} increased with the increased of Cu^{2+} initial concentration. When the initial concentration of Cu^{2+} was lower than 30 mg/L, the adsorption efficiency showed an increasing trend and remained above 90%. The maximum value was reached when the initial concentration of Cu^{2+} was 30 mg/L.

(3) The effect of solution pH on adsorption efficiency of Cu^{2+} ions: The experimental results were shown in Fig. 11.

The pH of the solution can affect the surface charge of the adsorbent and the existence state of Cu^{2+} ions, thereby influencing the adsorption of Cu^{2+} . From the figure, it could be observed that the adsorption rate of $\text{Fe}_3\text{O}_4@CTS/SBC$ composites Cu^{2+} in solution increased with the increased pH in the solution. The adsorption rate and adsorption capacity reached the maximum value at pH 5 and then began to decline.

(4) The effect of temperature on the adsorption efficiency of Cu^{2+} ions: The experimental results were shown in Fig. 12.

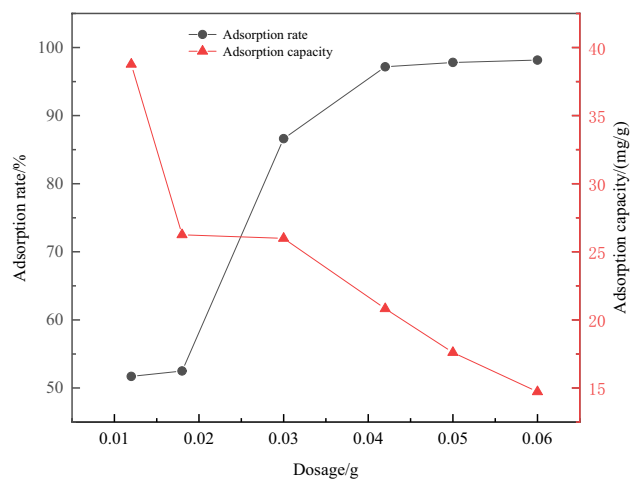


Figure 9. Influence of dosage on adsorption effect.

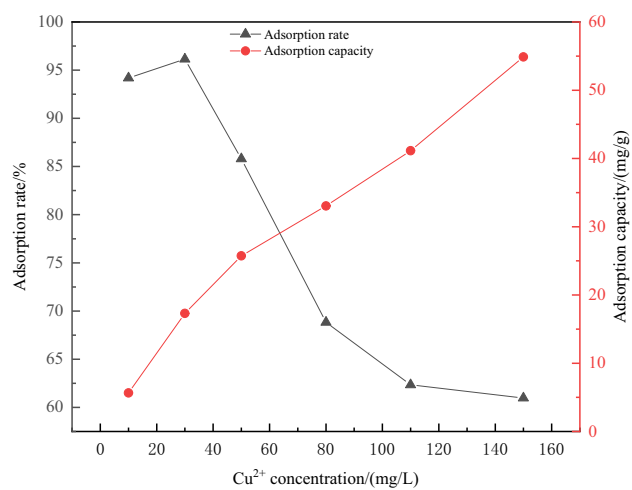


Figure 10. Effect of initial concentration of Cu^{2+} on adsorption effect.

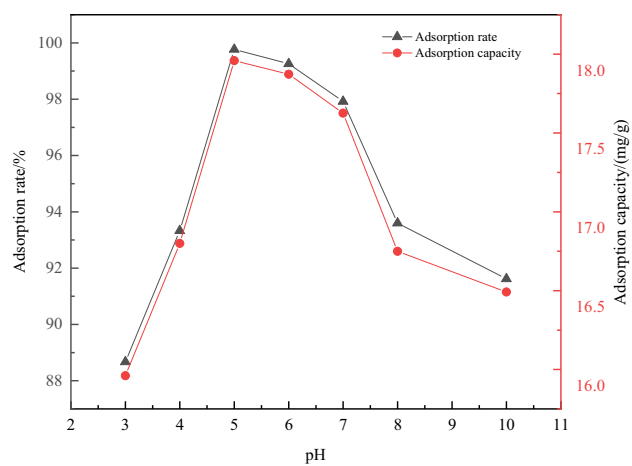


Figure 11. Effect of solution pH on adsorption of Cu^{2+} .

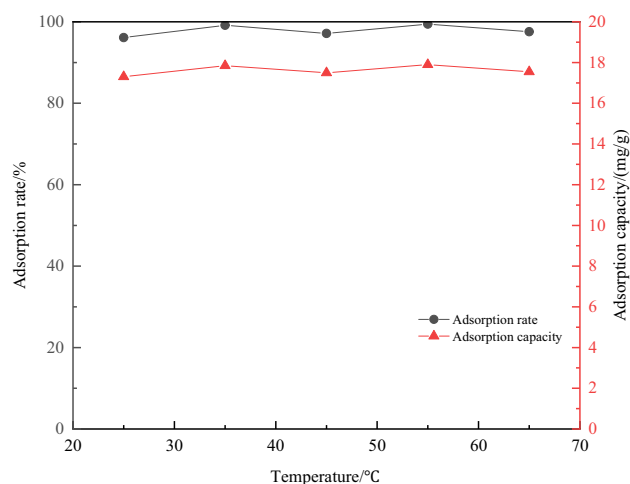


Figure 12. Effect of temperature on adsorption of Cu^{2+} .

From the figure, the adsorption efficiency of magnetic chitosan/sludge biochar was stable at about 90% with increasing temperature. The adsorption capacity also remained relatively stable. This indicated that the variation in temperature has little effect on the adsorption efficiency of the composites.

Adsorption performance evaluation

Adsorption kinetics research

When the adsorption conditions were $T = 298 \text{ K}$, $\text{pH} = 5$, Cu^{2+} concentration of 30 mg/L in 30 mL solution, and 0.5 g of $\text{Fe}_3\text{O}_4@\text{CTS}/\text{SBC}$ composites, the experimental data were fitted by using pseudo-first-order, pseudo-second-order kinetic models, intraparticle diffusion model and Boyd first-order dynamics model. The specific results were shown in Fig. 13a–d.

For a copper sulfate solution with an initial concentration of 30 mg/L , the adsorption rate of Cu^{2+} was very fast within 100 min and reached adsorption equilibrium around 200 min . Each gram of $\text{Fe}_3\text{O}_4@\text{CTS}/\text{SBC}$ composites could adsorb 17.9713 mg of Cu^{2+} , at which point the equilibrium concentration of Cu^{2+} in solution was 0.17 mg/L . The adsorption kinetics of Cu^{2+} were shown in Fig. 13, and the fitting results were shown in Table 2. From Fig. 13 and Table 2, it could be observed that Q_t/T showed a good linear relationship with T , and the R^2 value of 0.9982 . The saturated adsorption capacity was like to the experimental results, and the pseudo-second-order kinetics better was more in line with the adsorption of Cu^{2+} by the $\text{Fe}_3\text{O}_4@\text{CTS}/\text{SBC}$ composite adsorbent.

The intraparticle diffusion model was fitted with $t^{0.5}$ as the x -coordinate and Q_t as the y -coordinate. The fitting results were shown in Fig. 13c. The line in the figure did not pass through the origin, indicating that intra-particle diffusion was not the only step controlling the adsorption rate. Therefore, the adsorption of Cu^{2+} on $\text{Fe}_3\text{O}_4@\text{CTS}/\text{SBC}$ composite adsorbent could be divided into three stages. According to the fitting data in Table 2, the adsorption rate slowed down with increasing adsorption time.

The adsorption capacity of copper ions by 0.5 g composites combined with the linearized adsorption kinetics model (Eq. (6)), linearized fitted adsorption kinetic model could be obtained respectively (Fig. 13d, and the relevant parameters of the fitted line were shown in Table 2.

Adsorption isotherm research

The adsorption isotherms of $\text{Fe}_3\text{O}_4@\text{CTS}/\text{SBC}$ composite adsorbent were investigated for Cu^{2+} adsorption at constant temperature. The experiments were carried out at $25 \text{ }^\circ\text{C}$, $35 \text{ }^\circ\text{C}$, and $45 \text{ }^\circ\text{C}$, respectively. The Langmuir model, Freundlich model and Temkin model were used to fit the adsorption process. The initial concentration of Cu^{2+} was chosen to be in the range of $10\text{--}170 \text{ mg/L}$. Other adsorption conditions included $\text{pH} 5$, 0.5 g $\text{Fe}_3\text{O}_4@\text{CTS}/\text{SBC}$ composite adsorbent. The adsorption isotherms of Cu^{2+} were shown in Fig. 14a–c, and the fitted results were presented in Table 3.

The results showed that although the equilibrium concentration of Cu^{2+} (C_e) increased with the initial concentration, the equilibrium adsorption capacity (Q_e) of the adsorbent also increased. Linear regression analyses were performed on the isotherm data, and Fig. 14a,b showed the linear relationships between C_e/Q_e and C_e , as well as $\ln Q_e$ and $\ln C_e$. In Fig. 14a, Q_m and K_1 could be calculated, and the correlation coefficients R^2 at different temperatures were 0.8288 , 0.9735 , and 0.9719 , respectively, which were all closer to 1 than the Freundlich model. In this study, the Langmuir model was more suitable for the adsorption of Cu^{2+} by the $\text{Fe}_3\text{O}_4@\text{CTS}/\text{SBC}$ composite adsorbent. The average saturation adsorption capacities at the three temperatures were 65.89 mg/g , 70.60 mg/g , and 79.49 mg/g , which were very close to the calculated maximum adsorption capacities of 55.16 mg/g , 61.65 mg/g , and 71.07 mg/g , respectively. In addition, the Freundlich isotherm was fitted with n greater than 1, indicating that the adsorption process was easy to carry out. The Temkin isotherm model was well fitted, which indicated that the presence of electrostatic force for the adsorption of Cu^{2+} by $\text{Fe}_3\text{O}_4@\text{CTS}/\text{SBC}$.

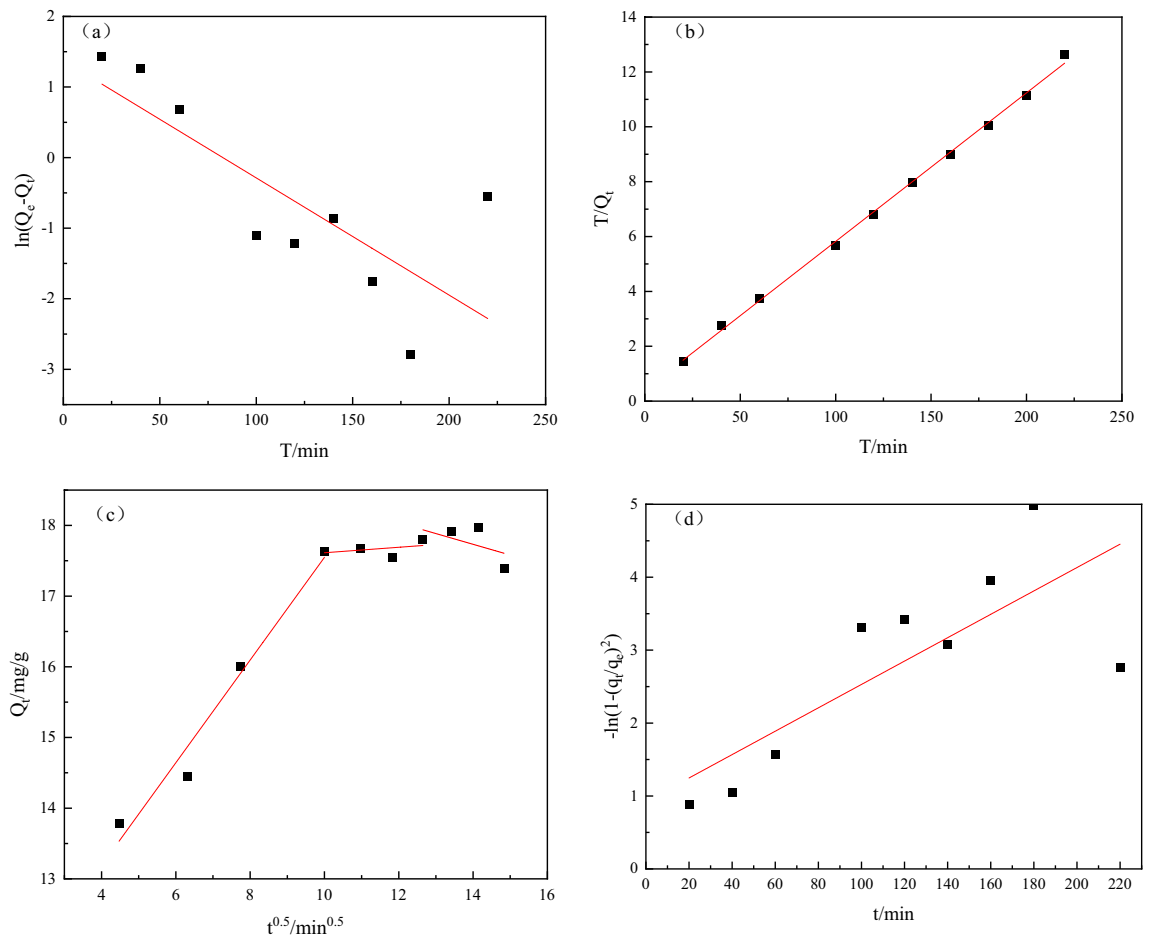


Figure 13. (a) Pseudo-first-order adsorption kinetic model (b) pseudo-second-order adsorption kinetic model, (c) Intraparticle diffusion model of Cu²⁺ adsorption (d) Boyd model of Cu²⁺ adsorption.

Adsorption kinetics models	
Simulating the concentration of Cu ²⁺ (mg/L) in wastewater	30
Q _{e,exp} /(mg/g)	17.9713
Pseudo-first-order kinetics	
k ₁ /(min ⁻¹)	0.0166
Q _e /(mg/g)	3.9476
R ²	0.6169
Pseudo-second-order kinetics	
k ₂ /(g/(mg min))	0.0072
Q _e /(mg/g)	18.4672
R ²	0.9982
Intraparticle diffusion model	
k _{p,1}	0.7264
k _{p,2}	0.0387
k _{p,3}	-0.1518
Boyd first-order dynamics model	
k _i	0.01603
R ²	0.6106

Table 2. Comparison of kinetic models for adsorption of Cu²⁺ by Fe₃O₄@CTS/SBC complex adsorbent.

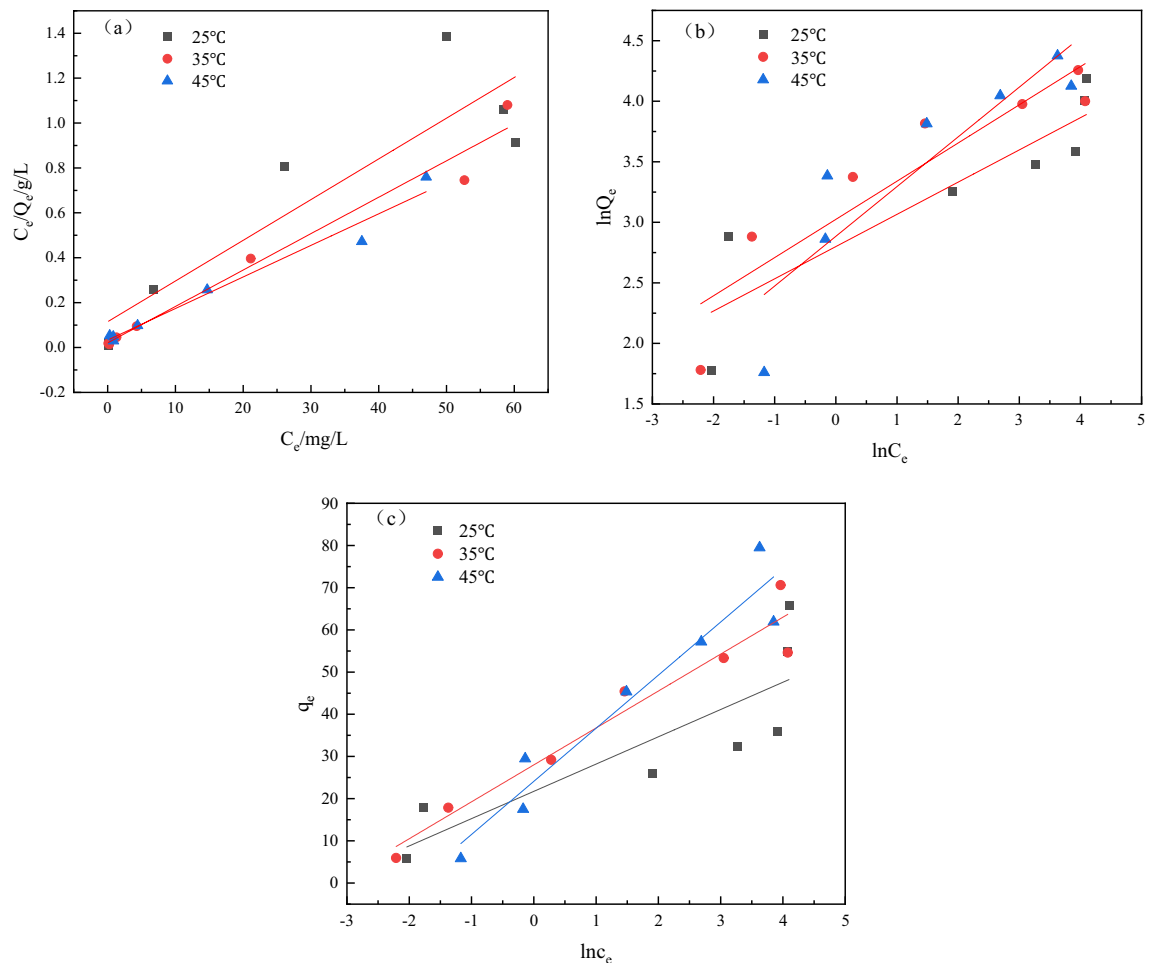


Figure 14. $\text{Fe}_3\text{O}_4@CTS/SBC$ (a) Langmuir (b) Freundlich (c) Temkin isotherm model for Cu^{2+} .

The isotherm equation	Parameters	Temperature/(K)		
		298	308	318
Langmuir	$Q_m/(\text{mg/g})$	55.16	61.65	71.07
	$K_L/(\text{L/mg})$	0.1579	0.7874	0.4268
	R^2	0.8288	0.9735	0.9719
Freundlich	$K_F/(\text{mg}^{1-1/n}\text{L}^{1/n}/\text{g})$	16.441	20.579	17.895
	n	3.76	3.17	2.44
	R^2	0.8081	0.8531	0.8108
Temkin	Kt	28.82	24.51	6.787
	b	375	286	205
	R^2	0.7199	0.9421	0.9272

Table 3. Langmuir, Freundlich and Temkin isotherm parameters of Cu^{2+} adsorption.

Adsorption thermodynamics research

The slope and intercept of the straight line obtained by $\ln k$ plotting $1/T$ gives ΔH and ΔS , and then ΔG . The results were shown in Table 4.

As shown in Table 4, $\Delta G < 0$, $\Delta H > 0$ of $\text{Fe}_3\text{O}_4@CTS/SBC$ adsorbent for Cu^{2+} indicated that the adsorption process was a spontaneous endothermic reaction. ΔS was greater than 0, which indicated that the adsorption of Cu^{2+} by the adsorbent was a process of entropy increased, and the chaos of the solid–liquid interface increased.

T/K	Thermodynamic parameter		
	ΔG /(kJ/mol)	ΔH /(kJ/mol)	ΔS /(kJ/mol/K)
298	-25.55	3.949	0.099
308	-26.54		
318	-27.53		

Table 4. Thermodynamic parameter.

Discussion

Instrumental analysis

In the XRD analysis of this study, the six diffraction peaks of Fe_3O_4 @CTS corresponding to ($2\theta = 30.1^\circ$, 35.5° , 43.1° , 53.5° , 57.0° , and 62.6°) by comparing them with the PDF standard card of Fe_3O_4 represent (220), (311), (400), (422), (511), and (440) respectively of the crystal surface^{28,29}. This indicated that magnetite has been successfully loaded onto the chitosan surface and magnetic chitosan has been successfully prepared. From the XRD spectrum of Fe_3O_4 @CTS/SBC, it could be seen that the Fe_3O_4 @CTS/SBC composites also exhibited the same diffraction peaks as Fe_3O_4 @CTS material. Additionally, the characteristic peaks of Fe_3O_4 remained at 37.1° and 66.9° , which indicated that Fe_3O_4 has been loaded onto the SBC. Furthermore, weak peaks were observed at 25.9° and 28.2° , which correspond to the diffraction peaks of chitosan (CTS) on the standard card, which indicated that CTS has been loaded onto SBC. This demonstrated the successful preparation of the Fe_3O_4 @CTS/SBC composites. The XRD spectrum of the Fe_3O_4 @CTS/SBC composites retained the main diffraction peaks of SBC, but the intensity was changed. This was due to the loading of CTS and Fe_3O_4 onto the surface of sludge biochar.

From the SEM analysis of this study, from Fig. 3, it could be observed that sludge biochar (SBC) had a rough wrinkled surface appearance and an abundant pore structure. This is due to the pore structure formed during the pyrolysis process in the tubular furnace, which gave SBC a certain adsorption capacity. Figure 4 showed that the morphology of the composites changed significantly compared to SBC. The Fe_3O_4 @CTS/SBC had a rough and porous surface with fewer macropores and a predominantly mesoporous structure. Visible white particles of magnetic nanoparticles were attached to the surface of SBC, which were adhered to the surface of SBC through chitosan. This indicated that Fe_3O_4 had been successfully loaded onto the surface of the biochar. These particles did not appear to be significantly aggregated, which indicated that the Fe_3O_4 particles could be uniformly dispersed on the biochar surface. The biochar could serve as an effective carrier, which was more conducive to adsorption.

The analysis of the adsorption–desorption isotherms using inert N_2 gas on SBC and Fe_3O_4 @CTS/SBC adsorbents indicated that both exhibited Type IV adsorption isotherms, which were typical for mesoporous materials. Additionally, a H_2 -type hysteresis return lines were observed. When $P/P_0 < 0.4$, SBC showed monolayer adsorption of N_2 , and the inflection point was followed by the end of monolayer adsorption and the beginning of multilayer adsorption. It could also be observed from the figure that the adsorption capacity of SBC on N_2 was low, while the adsorption capacity of Fe_3O_4 @CTS/SBC composite adsorbent was high. This indicated that the specific surface area of the composite adsorbent had increased.

According to Table 1, the specific surface area of Fe_3O_4 @CTS/SBC was 3.52 times larger than that of SBC, and the pore volume was increased by 2.17 times. The improvement in specific surface area was highly beneficial for enhancing the adsorption capacity of Fe_3O_4 @CTS/SBC. Furthermore, the introduction of chitosan introduced active functional groups such as $-\text{NH}_2$ and $-\text{OH}$ on the surface of the composite adsorbent, which further enhanced the interaction between the adsorbent and heavy metal ions.

Effect of parameters

From Fig. 9, with the increase in the dosage of the composites, the number of active groups bound to Cu^{2+} also increased, leading to an increase in the adsorption rate. However, when the dosage exceeded 0.03 g, the concentration of Cu^{2+} remained constant and the number of active groups involved in binding Cu^{2+} reached a critical value, resulting in a less significant increase in the adsorption efficiency³⁰. At the same time, it could be observed from the figure that the adsorption capacity of Cu^{2+} gradually decreased with the increased in the dosage of the material. This was because when the dosage of the adsorbent was low, the adsorption capacity of Fe_3O_4 @CTS/SBC composites for Cu^{2+} quickly reached saturation. However, continuing to increase the dosage led to more vacant binding sites on the surface of the adsorbent due to the fixed amount of adsorbate, which led to a decrease in the adsorption capacity. Based on the above analysis, 0.05 g was selected as the optimal dosage in this study.

As can be seen from Fig. 10, the adsorption capacity of Fe_3O_4 @CTS/SBC composites for Cu^{2+} increased with the increased in the initial concentration of Cu^{2+} . This was because as the initial concentration of Cu^{2+} increased, there were more adsorbates, resulting in a larger concentration difference between the solid and liquid phases, which provided a driving force for adsorption. In addition, with the increased of adsorbate quantity, the driving force increased, leading to an increase in the attraction between the adsorbate and adsorbent, which increased the adsorption capacity³¹. The adsorption efficiency showed an increasing trend when the Cu^{2+} initial concentration was lower than 30 mg/L, and it remained above 90%. The maximum point was reached at the initial concentration of Cu^{2+} of 30 mg/L. However, when the initial concentration of Cu^{2+} exceeded 30 mg/L, the adsorption efficiency of the material gradually decreased. This was because at lower Cu^{2+} concentrations, Fe_3O_4 @CTS/SBC composites provided more adsorption sites, which resulted in better adsorption efficiency. However, with the

increased of Cu^{2+} content in the solution, the adsorption sites on the surface of Fe_3O_4 @CTS/SBC composites gradually decreased during the adsorption process at a certain adsorbent addition amount. When the adsorption sites of the composites reached saturation, it no longer adsorbed Cu^{2+} , but the initial concentration of Cu^{2+} continued to increase. Therefore, the adsorption efficiency of the magnetic chitosan/sludge biochar composites decreased with the increased of the initial concentration of Cu^{2+} . In summary, the initial concentration of Cu^{2+} of 30 mg/L should be selected for subsequent experiments.

From Fig. 11, under acidic conditions, the amino groups of chitosan in the Fe_3O_4 @CTS/SBC composites mainly existed in the form of $-\text{NH}_3^+$, which repelled the positively charged divalent Cu^{2+} ions³². Meanwhile, under acidic conditions, the concentration of H^+ in water significantly increased. H^+ competed for the adsorption sites of the adsorbent with Cu^{2+} , which weakened the complexing ability of the composites towards Cu^{2+} ions³³. Therefore, under acidic conditions, the concentration of H^+ in water gradually decreased with the increase of pH, which led to the increase of adsorption efficiency. When the pH was greater than 6, Cu^{2+} ions in the copper solution easily formed precipitates in the form of $\text{Cu}(\text{OH})_2$, which led to a decrease in the adsorption efficiency. When the pH approached 7, chitosan was prone to coagulation, making it difficult to adsorb copper ions and resulting in a decrease in adsorption efficiency³⁴. Comparative experiments showed that when the pH of the solution was less than 6, Cu^{2+} was evenly distributed in the solution, and the magnetic composite material had a good adsorption performance for copper ions. When the pH was greater than 7, $\text{Cu}(\text{OH})_2$ precipitation would be formed, which interfered with the adsorption process and the adsorption performance began to decline. Therefore, based on the experimental data, the optimum pH for the adsorption of Cu^{2+} by the magnetic chitosan/sludge biochar composites was 5.

Comparative experiments showed that under the optimum conditions (initial concentration of Cu^{2+} = 30 mg/L, dosage of adsorbent = 0.05 g, solution pH 5, temperature = 25 °C), the removal of Cu^{2+} by Fe_3O_4 @CTS/SBC was 99.77%. The maximum adsorption capacity was 55.16 mg/g, while the removal rates of Fe_3O_4 @CTS and SBC for Cu^{2+} were 80.63% and 77.54%, respectively, which was much lower than the adsorption performance of the composites for copper ions, which indicated that the materials prepared in this experiment had better performance.

Adsorption kinetic analysis

The adsorption kinetics analysis indicated that the steps controlling the adsorption rate may be limited by chemisorption, which involved the sharing or exchanging electrons between the adsorbent and the adsorbate³⁵. The driving force of this process depended on the square of the adsorption sites³¹, which could explain the rapid adsorption rate at the initial stage of adsorption. However, in the later stage of adsorption, the reduction of adsorption sites on the Fe_3O_4 @CTS/SBC composite adsorbent and the decreased in Cu^{2+} concentration led to a decrease in the chemical driving force, which resulted in a slower adsorption rate³⁶.

The slopes of the three segments in the broken line were the particle diffusion rate constants $k_{p,1} > k_{p,2} > k_{p,3}$. The adsorption process of Cu^{2+} on Fe_3O_4 @CTS/SBC composite adsorbent could be described as follows: in the first stage of adsorption, Cu^{2+} combines with the adsorptive active sites of the functional groups on the surface of the Fe_3O_4 @CTS/SBC composite adsorbent, and the initial adsorption rate was fast³⁷. When the number of surface-active sites gradually decreased, it entered the second stage of adsorption. The adsorption sites on the surface of the Fe_3O_4 @CTS/SBC composite adsorbent were mainly occupied by Cu^{2+} , which began to enter the micropores of the composite adsorbent and was adsorbed by the micropores. At the third stage of adsorption, the adsorption sites on the surface and inside the pores of the Fe_3O_4 @CTS/SBC composite adsorbent were basically saturated, and the adsorption reached an equilibrium state³⁸. Based on the particle diffusion model, it could be concluded that the adsorption of Cu^{2+} by the Fe_3O_4 @CTS/SBC composite adsorbent was not only a chemical chelation, but also an intraparticle diffusion process.

The Boyd model is based on intraparticle diffusion rate control³⁹. The R^2 of Table 2 was 0.6106, which indicated that the model was poorly correlated. The intraparticle diffusion was not the only rate control step in the adsorption process of the Fe_3O_4 @CTS/SBC on copper ions, which was consistent with the findings of the intraparticle diffusion model. The Boyd model did not describe the adsorption of the Fe_3O_4 @CTS/SBC on copper ions well. In conclusion, the intraparticle diffusion model and the Boyd model can be useful to identify reaction pathways and adsorption mechanisms as well as to predict the rate-controlling step.

Adsorption isotherm analysis

The Freundlich model is more suitable for adsorption on highly heterogeneous surfaces lacking a saturated adsorption platform, in which case inhomogeneous processes occurred on the adsorbed surfaces and the adsorption process involved adsorption in multiple molecular layers⁷. The adsorption process in this study followed the Langmuir model. The Langmuir model assumes a monolayer adsorption effect, thus the Fe_3O_4 @CTS/SBC composite adsorbent exhibited monolayer adsorption, where only one molecule could be adsorbed at each active site, and all the adsorption sites had the same priority to form a homogeneous monolayer adsorption film⁴⁰.

Table 5 compared the removal effect of Fe_3O_4 @CTS/SBC composite adsorbent with the other adsorbents for the removal of Cu^{2+} under the room temperature conditions. Obviously, the Fe_3O_4 @CTS/SBC composite adsorbent showed better adsorption of 55.16 mg/g, which exceeded that of magnetite/carbon nanocomposites (41.11 mg/g)⁴¹, CS-SiO₂@TEuTTA luminous film (51.28 mg/g)⁴², DETA/SiO₂/Fe₃O₄ (13.459 mg/g)⁴³ and Dredged sludge-based adsorbent (40.62 mg/g)⁴⁴. Although there were adsorbents with excellent adsorption properties such as porous poly (lactic acid)/chitosan nanofibers (111.66 mg/g)⁴⁵, PS/Fe₃O₄/CS-PEI (204.6 mg/g)⁴⁶ and MCA-MCS-TiO₂ (220.67 mg/g)⁴⁷, these adsorbents were not favorable for production and application due to their complicated preparation process and high cost.

Adsorbent	Adsorption capacity/(mg/g)	References
Porous polylactic acid/chitosan nanofiber	111.66	Zia et al. ⁴⁵
Magnetite/carbon nanocomposite material	41.11	Andelescu et al. ⁴¹
Luminescent film CS-SiO ₂ @TEuTTA	51.28	Li et al. ⁴²
DETA/SiO ₂ /Fe ₃ O ₄	13.459	Chen et al. ⁴³
Dredged sludge-based adsorbent	40.62	Zhang et al. ⁴⁴
PS/Fe ₃ O ₄ /CS-PEI	204.6	Xiao et al. ⁴⁶
MCA-MCS-TiO ₂	220.67	Yu et al. ⁴⁷
Fe ₃ O ₄ @CTS/SBC composite adsorbent	55.16	This study

Table 5. Comparison of Cu²⁺ adsorption by Fe₃O₄@CTS/SBC complex adsorbent and other adsorbents.

Adsorption thermodynamic analysis

Literature^{48,49} suggested that the adsorbent-adsorbent interaction forces were hydrogen bonding, dipole attraction, van der Waals forces and chemical bonding when the values of $|\Delta H|$ are 2 ~ 40 kJ/mol, 2 ~ 29 kJ/mol, 4 ~ 10 kJ/mol, and greater than 60 kJ/mol, respectively. When the ΔG values were between - 20 ~ 0 kJ/mol and - 80 ~ 400 kJ/mol, the adsorption was physical adsorption and chemical adsorption, respectively. As can be seen from Table 4, the $|\Delta H|$ adsorbed by Fe₃O₄@CTS/SBC on Cu²⁺ is 3.949 kJ/mol, which indicated that there were hydrogen bonding and dipole moment attraction between Fe₃O₄@CTS/SBC adsorbent and Cu²⁺. The ΔG values for Cu²⁺ took values ranging from - 25.55 to - 27.53 kJ/mol, which indicated that the adsorption of Cu²⁺ by Fe₃O₄@CTS/SBC adsorbent was chemisorption.

Conclusion

In this study, a novel magnetic and recyclable biochar adsorbent was successfully synthesized using chitosan, Fe₃O₄, and sludge biochar as raw materials. The magnetic chitosan/sludge biochar composite adsorbent exhibited excellent adsorption performance for Cu²⁺. The maximum removal rate of 99.77% was achieved at an initial Cu²⁺ concentration of 30 mg/L, a dosage of 0.05 g of magnetic chitosan/sludge biochar composite, an adsorption time of 180 min, and a pH value of 5. Additionally, the maximum adsorption capacity was determined to be 55.16 mg/g at room temperature. The adsorption kinetics of Cu²⁺ by the magnetic chitosan/sludge biochar composite adsorbent followed the pseudo-second-order kinetic model. The adsorption isotherm conformed to the Langmuir isotherm model, which indicated that the adsorption process was monolayer chemisorption. As a novel and highly efficient adsorbent, Fe₃O₄@CTS/SBC has a great potential for the treatment of Cu²⁺ polluted wastewater. It has a wide material sources and economical preparation cost, making it a desirable option. Future research will focus on testing the effectiveness of the Fe₃O₄@CTS/SBC on other toxic heavy metals and metalloids, as well as mixed contaminants, through pilot-scaled tests. Additionally, the recovery performance of the adsorbent will be studied through regeneration experiments to evaluate its sustainability and reusability.

Received: 31 July 2023; Accepted: 6 November 2023

Published online: 28 November 2023

References

- Manne, R. *et al.* Water quality and risk assessment of copper content in drinking water stored in copper container. *Appl. Water Sci.* **12**(03), 27 (2022).
- Turan, K., Saygili Canlidinc, R. & Kalfa, O. M. Preconcentration of trace amount Cu(II) by solid-phase extraction method using activated carbon-based ion-imprinted sorbent. *Turk. J. Chem.* **46**(02), 550 (2022).
- Karthik, V. *et al.* Biochar production from Manilkara zapota seeds, activation and characterization for effective removal of Cu²⁺ ions in polluted drinking water. *Biomass Convers. Bioref.* **13**, 9381–9395 (2022).
- Senanu, L. D., Kranjac-Berisavljevic, G. & Cobbina, S. J. The use of local materials to remove heavy metals for household-scale drinking water treatment: A review. *Environ. Technol. Innov.* **29**, 103005 (2023).
- Raheem, S. A. *et al.* Study of using starch-modified chitosan for removal of phthalates from aqueous solution. *J. Water Chem. Technol.* **45**(01), 44–51 (2023).
- Chin, J. F., Heng, Z. W. & Pang, L. Y. Recent development of magnetic biochar crosslinked chitosan on heavy metal removal from wastewater-Modification, application and mechanism. *Chemosphere* **291**(03), 133035 (2022).
- Chao, L. *et al.* Preparation and adsorption properties of chitosan-modified magnetic nanoparticles for removal of Mo (VI) ions. *Pol. J. Environ. Stud.* **30**(03), 2489–2498 (2021).
- Zheng, L. W. *et al.* A novel, recyclable magnetic biochar modified by chitosan-EDTA for the effective removal of Pb(II) from aqueous solution. *Rsc Adv.* **10**(66), 40196–40205 (2020).
- Li, R. H. *et al.* Removal of cadmium(II) cations from an aqueous solution with aminothiourae chitosan strengthened magnetic biochar. *J. Appl. Polym. Sci.* **135**(19), 46239 (2018).
- Kang, X. D. *et al.* Study on the performance of sewage sludge biochar modified by nZVI to remove Cu(II) and Cr(VI) in water. *Water Sci. Technol.* **86**(07), 1821–1834 (2022).
- GB/T5750–2006. *Standard Test Method for Drinking Water.*
- Dong, X. Y. & Shi, L. W. Rapid determination of trace copper in rural drinking water by spectrophotometry with dicyclohexanone oxaldehydrazone. *Chin. J. Health Inspect.* **21**(4), 814–816 (2011).
- Yaqub, A. *et al.* Utilization of nano-biosorbents based on pine needles and banana peel for methylene blue removal: Equilibrium, kinetics, thermodynamic study, and application. *Biomass Convers. Bioref.* **12**(05), 1787–1802 (2022).

14. Bin Bandar, K. & Aljlil, S. Utilization of prepared nanocellulose as a biopolymer for adsorption kinetics of cobalt ions from wastewater. *Polymers* **15**(09), 2143 (2023).
15. Lu, W. S. *et al.* Adsorption and desorption characteristics of cadmium on different contaminated paddy soil types: Kinetics, isotherms, and the effects of soil properties. *Sustainability* **13**(13), 7052 (2021).
16. Saranya, M. *et al.* Batch kinetic studies of adsorption of Cu(II) ions from aqueous solutions onto alginate nanoparticles/PEG binary blend. *Indian J. Geo-Mar. Sci.* **51**(05), 484–489 (2022).
17. Boyd, G. E., Adamson, A. W. & Myers, L. S. The exchange adsorption of ions from aqueous solutions by organic zeolites H: Kinetics. *J. Am. Chem. Soc.* **69**(1), 2836–2848 (1947).
18. Jeppu, G. P. & Clement, T. P. A modified Langmuir-Freundlich isotherm model for simulating pH-dependent adsorption effects. *J. Contam. Hydrol.* **129**, 46–53 (2012).
19. Chen, Y. J. *et al.* Kinetics and isothermal adsorption of U(VI) in aqueous solution by nano-Ni-0. *J. Radioanal. Nucl. Chem.* **324**(01), 367–373 (2020).
20. Li, G. *et al.* Adsorption characteristics of Pb (II), Cd (II) and Cu (II) on carbon nanotube-hydroxyapatite. *Environ. Technol.* **42**(10), 1560–1581 (2021).
21. Vallejo, W., Diaz-Urbe, C. E. & Duran, F. Kinetic and thermodynamic study of methylene blue adsorption on TiO₂ and ZnO thin films. *Materials* **16**(12), 4434 (2023).
22. Zhu, Y. *et al.* Vibrational and structural insight into silicate minerals by mid-infrared absorption and emission spectroscopies. *Phys. Chem. Miner.* **49**(03), 6 (2022).
23. Chen, H. *et al.* Preparation of pickling-reheating activated alfalfa biochar with high adsorption efficiency for p-nitrophenol: Characterization, adsorption, behavior, and mechanism. *Environ. Sci. Pollut. Res.* **26**(15), 15300–15313 (2019).
24. Rao, X. *et al.* A comparison study of functional groups (amine vs. thiol) for immobilizing AuNPs on zeolite surface. *Nanomaterials* **9**(07), 1034 (2019).
25. Zhong, J. L. *et al.* Characteristic terahertz absorption spectra of paramylon and paramylon-ester compounds. *Spectrochim. Acta A* **244**, 118828 (2021).
26. Nazari, S., Mehri, A. & Hassannia, A. S. Fe₃O₄-modified graphene oxide as a sorbent for sequential magnetic solid phase extraction and dispersive liquid phase microextraction of thallium. *Microchim. Acta* **184**(9), 3239–3246 (2017).
27. Arán, D. *et al.* Influence of feedstock on the copper removal capacity of waste derived biochars. *Bioresour. Technol.* **212**, 199–206 (2016).
28. Lv, Z. *et al.* Nanoscale zero-valent iron/magnetite carbon composites for highly efficient immobilization of U(VI). *J. Environ. Sci.* **76**, 377–387 (2019).
29. Lyu, H. *et al.* Removal of hexavalent chromium from aqueous solutions by a novel biochar supported nanoscale iron sulfide composite. *Chem. Eng. J.* **322**, 516–524 (2017).
30. Matias, P. M. C. *et al.* Reduced chitosan as a strategy for removing copper ions from water. *Molecules* **10**, 4110 (2023).
31. Wu, J. *et al.* Hydrothermal carbonization synthesis of cassava slag biochar with excellent adsorption performance for Rhodamine B. *J. Clean. Prod.* **251**, 119717 (2020).
32. Shi, Z. *et al.* Adsorption of Cu²⁺ using magnetic chitosan/bentonite composite. *Chem. J. Environ. Eng.* **9**(12), 5677–5682 (2015).
33. Arar, O. Co-precipitative preparation of a sulfonated cellulose-magnetite hybrid sorbent for the removal of Cu²⁺ ions. *Anal. Sci.* **36**(01), 81–86 (2020).
34. Zhu, X. *et al.* Synthesis of magnetic rectorite/humic acid/chitosan composite for removal of heavy metal ions from water. *Desalin. Water Treat.* **163**, 155–165 (2019).
35. Lian, J. *et al.* Enhanced adsorption of molybdenum (VI) onto drinking water treatment residues modified by thermal treatment and acid activation. *J. Clean. Prod.* **244**, 118719 (2020).
36. Tu, Y. J. *et al.* XANES evidence of molybdenum adsorption onto novel fabricated nano-magnetic CuFe₂O₄. *Chem. Eng. J.* **244**(15), 343–349 (2014).
37. Baqer, Y. & Chen, X. H. A review on reactive transport model and porosity evolution in the porous media. *Environ. Sci. Pollut. Res.* **29**(32), 47873–47901 (2022).
38. Leon-Cazares, F. D. & Galindo-Nava, E. I. General model for the kinetics of solute diffusion at solid-solid interfaces. *Phys. Rev. Mater.* **5**(12), 123802 (2022).
39. Crank, J. *The Mathematics of Diffusion* (Clarendon Press, 1975).
40. Afkhami, A. *et al.* Effectiveness of Ni_{0.5}Zn_{0.5}Fe₂O₄ for the removal and preconcentration of Cr (VI), Mo (VI), V(V) and W(VI) oxyanions from water and wastewater samples. *J. Iran Chem. Soc.* **12**(11), 2007–2013 (2015).
41. Andeleescu, A. *et al.* Adsorption studies on copper, cadmium, and zinc ion removal from aqueous solution using magnetite/carbon nanocomposites. *Sep. Sci. Technol.* **53**(15), 2352–2364 (2018).
42. Li, L. *et al.* Luminescent CS-SiO₂@TEuTTA membrane for simultaneous detection and adsorption of copper(II) ions. *J. Environ. Chem. Eng.* **11**(02), 109573 (2023).
43. Chen, H. W. & Chang, S. H. Magnetic nanoadsorbents with amino-functionalized polymers for magnetic separation removal of copper ion. *Environ. Technol.* **43**(06), 805–814 (2022).
44. Zhang, R. X. *et al.* Preparation of dredged sludge-based adsorbent and its adsorption of copper ion in water. *New Chem. Mater.* **50**(01), 217–221 (2022).
45. Zia, Q. *et al.* Porous poly (L-lactic acid)/chitosan nanofibers for copper ion adsorption. *Carbohydr. Polym.* **227**, 115343 (2020).
46. Xiao, C. W. *et al.* Sub-micron-sized polyethylenimine-modified polystyrene/Fe₃O₄/chitosan magnetic composites for the efficient and recyclable adsorption of Cu(II) ions. *Appl. Surf. Sci.* **394**, 378–385 (2017).
47. Yu, H. *et al.* Separation of oil-water emulsion and adsorption of Cu (II) on a chitosan-cellulose acetate-TiO₂ based membrane. *Chemosphere* **235**, 239–247 (2019).
48. Yongmei, W. *et al.* Preparation of microscale zero-valent iron-fly ash-bentonite composite and evaluation of its adsorption performance of crystal violet and methylene blue dye. *Environ. Sci. Pollut. Res.* **24**, 1–13 (2017).
49. Oepen, B. V., Kördel, W. & Klein, W. Sorption of nonpolar and polar compounds to soils: Processes, measurements and experience with the applicability of the modified OECD-Guideline 106. *Chemosphere* **22**(3–4), 285–304 (1991).

Acknowledgements

The authors greatly acknowledge the financial support from the Key Laboratory Projects in Pollutant Chemistry and Environmental Governance (2022HJYB04), Special Project to Enhance the Comprehensive Strength of Disciplines at Yili Normal University (22XKZZ04) and Regional Science Foundation Project of National Natural Science Foundation of China (22366038).

Author contributions

(1) Design of experimental protocols and writing of articles: M.Z.; (2) Maintenance of experimental instruments: Y.L. and Z.Y.; (3) Characterization and testing of experimental materials: D.F.; (4) Conducting experiments and data processing: H.L.

Competing interests

The authors declare no competing interests.

Additional information

Supplementary Information The online version contains supplementary material available at <https://doi.org/10.1038/s41598-023-46815-4>.

Correspondence and requests for materials should be addressed to Y.L. or Z.Y.

Reprints and permissions information is available at www.nature.com/reprints.

Publisher's note Springer Nature remains neutral with regard to jurisdictional claims in published maps and institutional affiliations.



Open Access This article is licensed under a Creative Commons Attribution 4.0 International License, which permits use, sharing, adaptation, distribution and reproduction in any medium or format, as long as you give appropriate credit to the original author(s) and the source, provide a link to the Creative Commons licence, and indicate if changes were made. The images or other third party material in this article are included in the article's Creative Commons licence, unless indicated otherwise in a credit line to the material. If material is not included in the article's Creative Commons licence and your intended use is not permitted by statutory regulation or exceeds the permitted use, you will need to obtain permission directly from the copyright holder. To view a copy of this licence, visit <http://creativecommons.org/licenses/by/4.0/>.

© The Author(s) 2023